# 3D Surface Acquisition for FMT Using High-Accuracy Fringe Projection Profilometry

Juan E. Ortuño, Pedro Guerra, *Member, IEEE*, George Kontaxakis, *Senior Member, IEEE*, María J. Ledesma-Carbayo, *Member, IEEE*, and Andrés Santos, *Senior Member, IEEE*

*Abstract*–An experimental structured light projection system which includes a miniaturized projector is described. The system has been designed to be integrated in a fluorescence molecular tomography (FMT) prototype in order to reconstruct the surface of mice and phantom studies. A high-accuracy phase map is retrieved with phase-shifted sinusoidal fringes. Phase error due to the nonlinear gamma function of the pico-projector is calibrated and compensated. Robust phase unwrapping is performed with an additional Gray-code projection sequence. An automatic phase-to-height non-linear calibration scheme has been applied using objects located in the extremes of the field of view. The accuracy of the proposed method has been tested with a realistic mouse model and ray-tracing software.

## I. INTRODUCTION

FLUORESCENCE molecular tomography (FMT) is a biomedical imaging technique that quantifies the distribution of fluorescent biomarkers in small animals (e.g., mice) [1]. Tomographic reconstruction of fluorophore distribution at depths of several millimeters to centimeters has been possible thanks to the emergence of mathematical models that describe photon propagation in biological tissues [2]. FMT has been largely limited to configurations with slab geometry and optical fibers in physical contact with tissues, where the animal is compressed and immersed into a chamber filled with an optically diffusive matching fluid [3]. This scheme creates additional photon diffusion and attenuation, and is not always feasible or desirable for in vivo studies. To overcome these limitations, FMT of small animals using free-space surface detection schemes has been proposed [4]. These setups need to acquire the 3D surface of the mouse and it has been reported that sub-millimeter precision is desirable for accurate quantitative measurements [5].

Structured light (or fringe projection) 3D surface acquisition methods are widely applied for multiple applications [6]. A typical structured light 3D measurement system consists of a camera and a digital projector, which projects a series of stripes or another type of coded patterns onto the object. The camera records the distorted patterns caused by the variations of heights relative to the reference plane. The 3D surface can then be reconstructed based on triangulation once the system is properly calibrated.

In this paper, we propose the integration of a fringe pattern projection system in a compact FMT prototype using miniaturized digital projectors to acquire the 3D shape of mice and phantom studies.

## II. MATERIALS AND METHODS

The structured light projection system has been designed to be integrated in a novel FMT CCD camera based system that works in non-contact geometry [7]. The light emitted by the fluorophore is captured with a CCD camera located on top of the scanner and mechanically fixed to the system cabinet in the way that the focal plane is parallel to the reference plane where the mouse is placed.

An experimental setup was mounted to test the proposed code light projection system (Fig. 1) prior to the integration with the FMT prototype. The assembly consist of a low-cost CCD camera (Sony DSC-W1) placed in the top of the device and a pico-projector (model PK101, Optoma Technology, Inc) with DLP® technology (Texas instruments, Inc.). The pico-projector has a minimum focus range of 210 mm, angular aperture of 35º and HGVA resolution. The setup has dimensions of 20×30×30 cm, appropriate to be further integrated in the FMT prototype, replacing the DSC-W1 camera by the electron-multiplier CCD camera also used to collect fluorescent emissions.
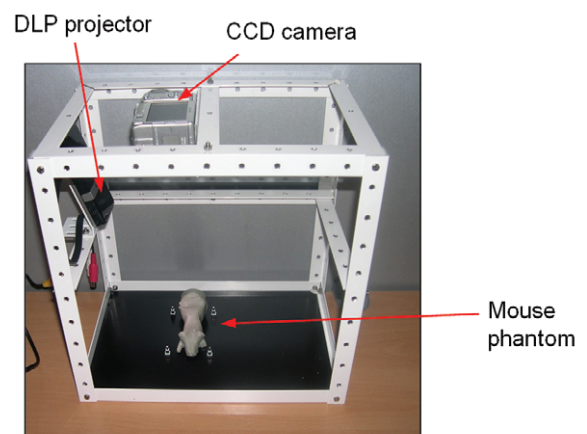


Fig. 1. Experimental setup mounted to test the proposed coded light projection system. The device is composed of a DLP pico-projector and a CCD camera that collects deformed patterns reflected by the object.

In addition to acquisitions using the experimental setup, a realistic ray-tracing simulation was carried out using Persistence of Vision™ Raytracer (version 3.6) software [8]. Simulation includes gamma nonlinearity effect of pico-projector, shadows, reflections and albedo differences.

### A. Fringe pattern projections

In each acquisition, four sinusoidal patterns $g_i$ with phase shifts of 90º are projected:

$$g_i(x,y) = a(x,y) + b(x,y)\cos\left(\varphi(x,y) + \frac{\pi}{2}i\right), \ i = 0,1,2,3 \quad (1)$$

where $a$ is the average intensity and $b$ is the modulation in each point coordinate $(x,y)$. Wrapped phase $\varphi$ is solved with:

$$\varphi(x,y) \bmod \pi = \arctan\left(\frac{g_4 - g_2}{g_3 - g_1}\right) \quad (2)$$

Phase error due to the gamma function of the DLP pico-projector is compensated with a calibration look-up-table [9]. Phase unwrapping is performed with an additional Gray-code sequence of 5 bits, which is robust to ambiguities in surface discontinuities. The sequence of patterns, including a full illuminated image is shown in Fig. 2 in the case of a Ray-tracing simulation of a mouse model.



Gray code sequence

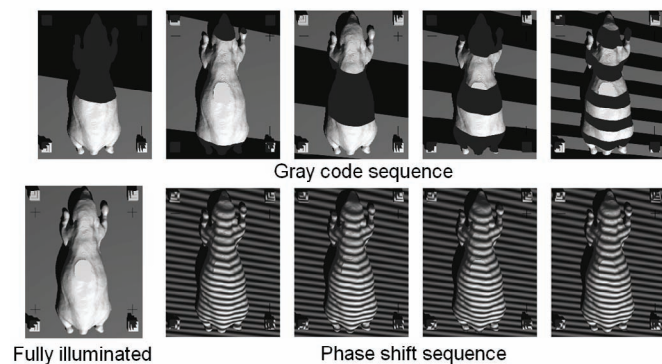Fully illuminated          Phase shift sequence

Fig. 2. Ray-tracing simulation of mouse model, showing the structured light patterns.

Phase of reference plane in occluded areas (e.g., below the mouse) is extrapolated from surrounding values using polynomial splines, so there is no need to perform a dedicated background acquisition to repeat background acquisitions. Occluded and shaded zones can be reduced repeating the sequence of structured pattern projections at two different pico-projector orientations. For not occluded or shadowed pixels, the height is calculated as the mean value of the two results.

### B. System calibration

The correspondence between phase values and height over the reference plane is calculated with empirical methods that not need to know the extrinsic (i.e., location and orientation) and optical parameters of the pico-projector. In this work we propose novel automatic nonlinear calibration method that simplifies the phase-to-height mapping process. Nonlinear and

linear empirical non-automatic calibrations have been also tested. Nonlinear phase-to-height mapping [10] is calculated as:

$$h(x,y) = \frac{\Delta\varphi(x,y)}{m(x,y) + n(x,y)\Delta\varphi(x,y)} \quad (3)$$

where $h(x,y)$ is the height over the reference plane in the $(x,y)$ point, $\Delta\varphi$ is the unwrapped phase difference between the object and the reference plane, and $(m,n)$ are the parameters obtained with a least squares minimization algorithm [11]. This calibration procedure, denoted from now on, as calibration #1 for short, requires of the acquisition of at least two planar slabs of different height.

Linear phase-to-height mapping, denoted from now on as calibration #2, is calculated as:

$$h(x,y) = k(x,y)\Delta\varphi(x,y) \quad (4)$$

In theory, this approach only requires one calibration acquisition to guess the parameter $k(x,y)$. However in practice several measurements are performed to increase the accuracy.

The novel automatic phase-to-height mapping presented in this work is based on calibration #1 and assumes that parameters $m$ and $n$ in (3) have smooth and quasi-linear variation along $(x,y)$. This assumption enables estimating their value from a set of four measurements located in the extremes of the field of view. This method is denoted as calibration #3.
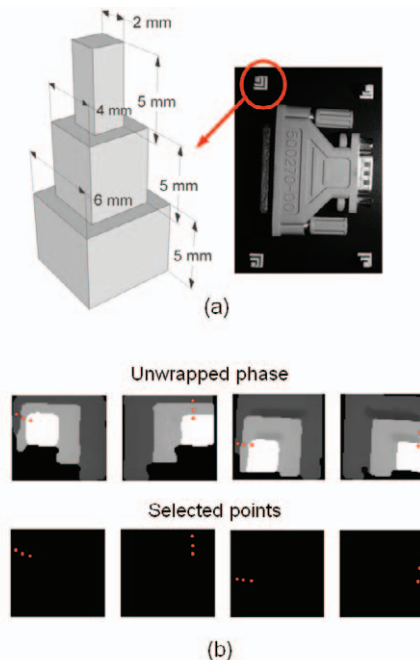


Unwrapped phase

Selected points

(b)

Fig. 3. (a) Stepped pyramid-shaped calibration objects situated together with the object to be measured; (b) detail of unwrapped phase of stepped pyramidal objects and selected points used to non linear calibration marked in red color.

Stepped pyramid-shaped objects were selected as calibration objects. The shape of the objects guarantees that it will be different heights at nearby locations and will be visible (i.e., no shadowed) for every pico-projector orientation. We have used steps of 2 mm wide and 5, 10 and 15 mm height, in four step-pyramids located, as is shown in Fig. 3a. The

segmentation of pyramid-shaped objects is a fully automatic process that includes simple but robust histogram-based segmentation and morphological operations. A detail of unwrapped phase of stepped pyramidal objects and selected points used in calibration is shown in Fig. 3b.

Interpolation of calibration parameters over the rest of the image is performed with a Delaunay triangulation followed by a smooth quintic polynomial interpolation.

Camera calibration is needed for perspective correction (i.e., correction of x-y locations over the reference plane after height estimation). Camera calibration algorithm obtains intrinsic and extrinsic parameters for the pinhole camera model using the Zhang method [12]. The procedure employs a checkerboard patterns placed at different and unknown orientations. Camera calibration only needs to be calculated when the camera, fixed on the top of the setup, is moved or zoomed. Perspective correction does not depend of the pico-projector orientation.

## III. RESULTS

### A. Ray-tracing models

Accuracy of the proposed methodology has been tested with simulated acquisitions of a phantom shown in Fig. 4b, composed of 19 steps with height ranges from 1 to 19 mm.
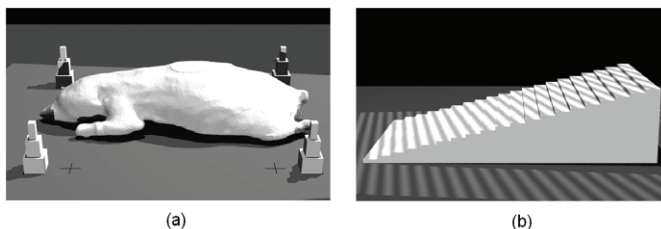


Fig 4. (a) PovRay Rendering of mouse model and stepped pyramid-shapped calibration objects; (b) phantom used to test the accuracy of algorithms, composed of steps of 1 mm height.

Four different acquisitions were done changing polar deflection θ and azimuthal angle φ of the projected fringes: Projection #a: θ=30º, φ=−25º; projection #b: θ=30º, φ=165º; projection #c: θ=15º, φ=30º; and projection #d: θ=25º, φ=195º. Root mean squared error (RMSE) of average measured heights in each step is shown in Fig. 5. The upper plot shows results for each pico-projector position using calibration #3, while the lower plot shows the mean value of RMSE over the four projections with calibrations #1, #2 and #3. Three slabs of 5, 10 and 15 mm height were employed in calibrations #1 and #2.

Mean RMSE in inferior to 5 μm for calibration #1 in the range of 0-20 mm height, equal to 146 μm for calibration #2, and 62 μm for calibration #3. The maximum RMSE with calibration #3 is of 125 μm at 13 mm height but linear calibration #2 reached a maximum RMSE of 0.44 mm at 19 mm height.

The mouse surface model shown in Fig. 4a was obtained from a 3D mouse atlas of CT data [13]. The voxellized data had 330×890×200 voxels (0.1 mm/voxel). The external 3D surface used in rendered scenes was calculated with Delaunay

triangulation ($2×10^5$ triangles). The combination of projection #a and #d was used in order to minimize shaded regions. A rendering of the 3D surface is shown in Fig 6c.
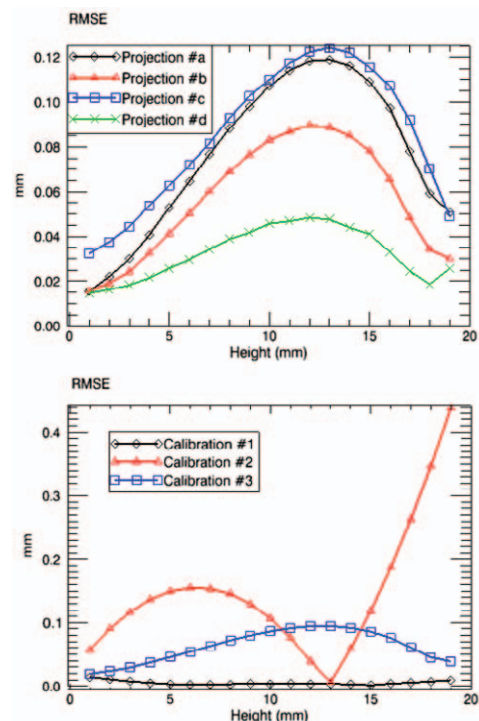


Fig. 5. Upper plot: Root mean square error (RMSE) in four pico-projector locations with nonlinear calibration #3; lower plot: RMSE mean of four pico-projector locations using calibrations #1, #2 and #3.

According to plot of Fig. 5, error with calibration #1 is negligible in the range of 0-20 mm height, so the differences of height obtained with this method with respect calibrations #2 and #3 can be considered as an indicator or accuracy of the former methods. Root mean squared difference of measured heights in the mouse surface model between calibration #1 and #3 and between calibration #1 and #2 can be observed in Fig. 6a-b. The mean values are 58 μm and 192 μm, respectively.
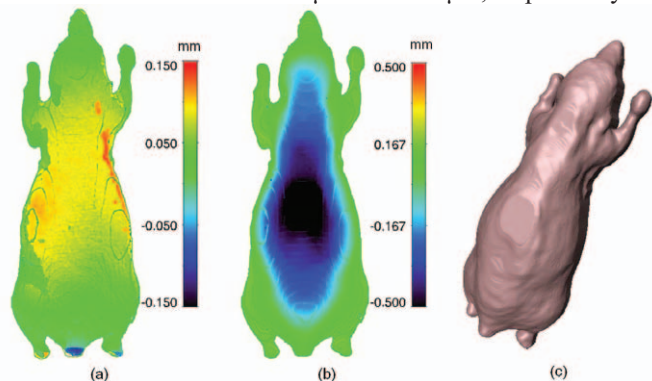


Fig. 6. Mouse surface model: (a) Height difference of calibration #3 with respect to calibration #1; (b) height difference of calibration #2 with respect to calibration #1; (c) rendering of result using calibration #3.

### B. Experimental setup

Slabs 4, 8, 12 and 16 mm height were used to calibrate the experimental setup for methods #1 and #2. The acquisitions of

these slabs were also employed to evaluate the accuracy of calibration method #3. Table 1 compares the RMSE using calibration #2 and #3.

TABLE 1. HEIGHT ERRORS IN SLABS OF CONSTANT HEIGHT

| Height | 4 mm | 8 mm | 12 mm | 16 mm |
|---|---|---|---|---|
| RMSE (µm), method #2 | 256 | 215 | 48 | 193 |
| RMSE (µm), method #3 | 76 | 128 | 113 | 99 |

Fig.7 shows the reconstructed 3D shape of an agar mouse phantom and a computer adapter. One pico-projector was used in these cases so there are shadowed zones. Problematic shiny surfaces were eliminated in this result.
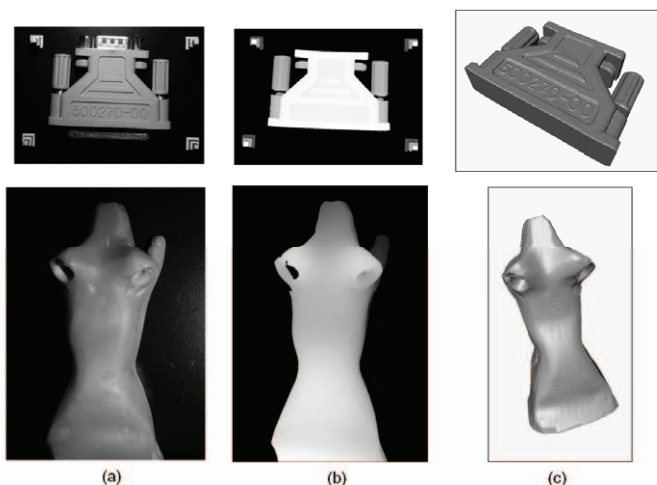


Fig. 7. (a) Full illuminated scene of computer adapter and agar mouse phantom; (b) height map with one projection set. Shaded surfaces are not detected and metallic parts have been eliminated to avoid errors; (c) 3D rendering of reconstructed shapes.

## IV. CONCLUSSIONS

We have developed a surface reconstruction method in order to be integrated in a novel FMT compact camera which includes a miniaturized DLP pico-projector and a CCD camera. A novel and automatic phase-to-height calibration method has been proposed and compared together with linear and nonlinear empirical methods. A sub-millimetric accuracy was reported in realistic ray-tracing simulations as well as in the experimental setup.

According to results, nonlinear calibration shows superior performance but at the expense of needing additional acquisitions. In contrast, linear calibration showed poor results in both simulations and experimental setup results. The proposed automatic calibration algorithm shows RMSE below 0.1 mm, accurate enough for FMT surface requirements. Additional error introduced with this method is acceptable for FMT purposes, simplifying the acquisition protocol by placing small calibration artifacts with the mouse. We will employ this methodology to allow high resolution spatial sampling of photons in FMT.

REFERENCES

[1] V. Ntziachristos, "Fluorescence molecular imaging," *Annual Review of Biomedical Engineering*, vol. 8, pp. 1-33, 2006.

[2] V. Ntziachristos, J. Ripoll, L. H. V. Wang, and R. Weissleder, "Looking and listening to light: the evolution of whole-body photonic imaging,", *Nature Biotechnology*, vol. 23, no. 3, pp. 313-320, 2005.

[3] G. Zacharakis, J. Ripoll, R. Weissleder, and V. Ntziachristos, "Fluorescent protein tomography scanner for small animal imaging," *IEEE Trans. Med. Imaging* vol. 24, no. 7, pp 878-885, 2005.

[4] X. L. Song, D. F. Wang, N. G. Chen, J. Bai, and H. Wang, "Reconstruction for free-space fluorescence tomography using a novel hybrid adaptive finite element algorithm," *Optics Express,* vol. 15, no. 26, pp. 18300-18317, 2007.

[5] V. Ntziachristos, E. Graves, R. Schultz, and J. Ripoll, "Fluorescence molecular tomography: new detection schemes for acquiring high information content measurements," *Biomedical Imaging: Nano to Macro, 2004. IEEE International Symposium on*, vol. 2, pp. 1475-1478, 2004.

[6] F. Blais, "Review of 20 years of range sensor development," *Journal of Electronic Imaging*, vol. 13, no. 1, pp. 231-243, 2004.

[7] J. Aguirre, M. Abella, J. Ripoll, J. J. Vaquero, and M. Desco, "OSEM reconstruction algorithm for fluorescence molecular tomography: a preliminary Study," *International Journal of Computed Assisted Radiology and Surgery*, vol. 3, supplement 1, pp. S15-16, 2008.

[8] Persistence of Vision Pty. Ltd., Williamstown, Victoria, Australia. http://www.povray.org/

[9] S. Zhang, and P. S. Huang, "Phase error compensation for a 3-D shape measurement system based on the phase-shifting method," *Optical Engineering*, vol. 46, no. 6, pp. 63601-63610, 2007.

[10] P. R. Jia, J. Kofman, and C. English, "Comparison of linear and nonlinear calibration methods for phase-measuring profilometry," *Optical Engineering*, vol. 46, no. 4, pp. 3601-3610, 2007.

[11] H. W. Guo, H. T. He, Y. J. Yu, and M. Y. Chen, "Least-squares calibration method for fringe projection profilometry," *Optical Engineering*, vol. 44, no. 3, pp. 33603, 2005.

[12] Z. Zhang, "Flexible Camera Calibration by Viewing a Plane from Unknown Orientations," *Seventh International Conference on Computer Vision* (ICCV'99), vol. 1, pp. 666, 1999.

[13] B. Dogdas, D. Stout, A. F. Chatziioannou, and R. M. Leahy, "Digimouse: a 3D whole body mouse atlas from CT and cryosection data," *Physics in Medicine and Biology*, vol. 52, no. 3, pp. 577-587, 2007.